

PARAMETRIC SCATTERING NETWORKS

Shanel Gauthier^{1,3} Benjamin Thérien^{2,3} Laurent Alsène-Racicot^{1,3}
 Irina Rish^{1,3} Eugene Belilovsky^{2,3} Michael Eickenberg⁴ Guy Wolf^{4,3}

¹ Université de Montréal; ² Concordia University; ³ Mila – Quebec AI Institute, Montreal, QC, Canada
⁴ Flatiron Institute, New York, NY, USA

ABSTRACT

The wavelet scattering transform creates geometric invariants and deformation stability from an initial structured signal. In multiple signal domains it has been shown to yield more discriminative representations compared to other non-learned representations, and to outperform learned representations in certain tasks, particularly on limited labeled data and highly structured signals. The wavelet filters used in the scattering transform are typically selected to create a tight frame via a parameterized mother wavelet. Focusing on Morlet wavelets, we propose to instead adapt the scales, orientations, and slants of the filters to produce problem-specific parametrizations of the scattering transform. We show that our learned versions of the scattering transform yield significant performance gains over the standard scattering transform in the small sample classification settings, and our empirical results suggest that tight frames may not always be necessary for scattering transforms to extract effective representations.

Index Terms— scattering transform, wavelets, convolutional network, small sample classification

1. INTRODUCTION

The scattering transform, proposed in [1], is a cascade of wavelets and complex modulus nonlinearities, seen as a convolutional neural network (CNN) with fixed predetermined filters. This construction can be used to build representations with geometric invariants and is shown to be stable to deformations. It has been shown to yield impressive results on problems involving highly structured signals [2], outperforming a number of other classic signal processing techniques.

Since scattering transforms can be seen as CNN instantiations, they have been studied as a mathematical model for understanding the impressive success of CNNs in image classification [2, 3]. As discussed in [2], first order scattering coefficients are similar to SIFT descriptors [4], and higher order scattering can provide insight into the information added with depth. Moreover, theoretical and empirical study of information encoded in scattering networks indicates they often pro-

mote linear separability, which in turn leads to effective representations for downstream classification tasks [2, 5, 6, 7].

Scattering-based models have been shown useful in several applications involving scarcely annotated or limited labelled data [7, 8, 9]. Indeed, most breakthroughs in deep learning in general, and CNNs in particular, involve significant effort in collecting massive amounts of well annotated data to be used when training deep overparameterized networks. However, while big data have become increasingly prevalent nowadays, there are numerous applications (e.g., in biomedical and healthcare domains) where the task of annotating more than a small amount of samples is infeasible, which gave rise to increasing interest in small sample learning tasks and deep learning approaches towards them [10]. Recent work has shown that in image classification, state of the art results can be achieved by hybrid networks that harness the scattering transform as their early layers followed by learned layers based on a wide residual network architecture [9]. Here, we further advance this research avenue by proposing to use the scattering paradigm not only as fixed preprocessing layers in a concatenated architecture, but also as a parametric prior to learned filters learned in a CNN.

To formulate parametric scattering priors, we recall that the scattering construction is based on complex wavelets, generated from a mother wavelet via several operations, such as dilations and rotations, aimed to cover the frequency plane, while having the capacity to encode informative variability in input signals [2]. Further, discrete parametrization and indexing of these operations (i.e., by dilation scaling or rotation angle) have traditionally been carefully constructed to ensure the resulting filter bank forms an efficient tight frame with well established energy preservation properties. Here, we relax these constructions to allow data-driven learning (i.e., via backpropagation) of the wavelet parameters used in scattering layers of hybrid architectures¹, as discussed in Sec. 2.

To our knowledge, this is the first work that aims to learn the wavelet filters of scattering networks, and more generally to pose strict parametric priors on filters learned in early layers of convolutional networks, which have often been observed to resemble wavelets but not explicitly parameterized as such. Our empirical study, described in Secs. 3-4, evaluates our parametric scattering approach on three datasets and demonstrates its advantages in limited labelled data settings.

This research was partially funded by NSERC CGS-M [S.G., L.A.] and URA [B.T.] scholarships; NSERC Discovery Grant [E.B.]; IVADO PRF Grant [I.R., E.B., G.W.]; and CIFAR AI Chairs [I.R., G.W.]. The content is solely the responsibility of the authors and does not necessarily represent the official views of funding agencies. Correspondence to <guy.wolf@umontreal.ca>

¹Code available on <https://github.com/bentherien/ParametricScatteringNetworks>

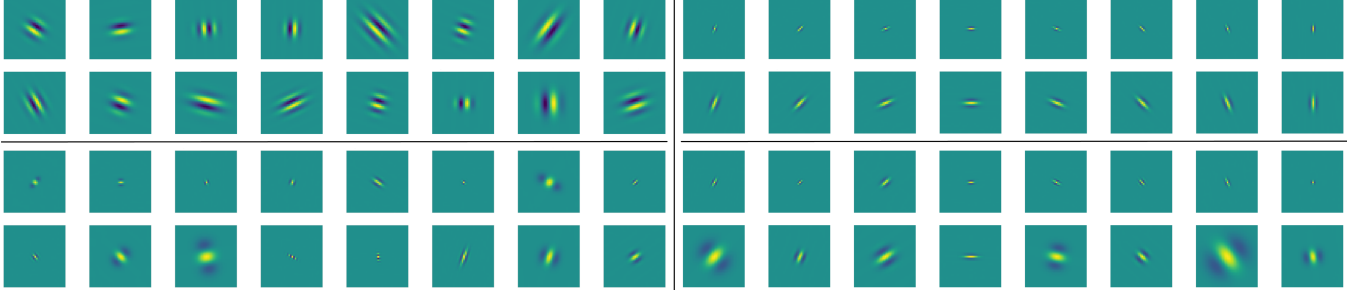


Fig. 1. Real part of Morlet wavelet filters initialized with *random* (left) and *tight frame* (right) schemes before (top) and after (bottom) training. The filters were optimized on the entire CIFAR-10 training set with linear model. For the tight frame filters, we observe substantial changes in both scale and slant. However, orientations are less perturbed. On the other hand, all random filters undergo major changes in orientation and scale.

2. PARAMETRIC SCATTERING NETWORKS

To introduce parametric scattering networks, we first revisit the formulation of traditional scattering convolution networks in Sec. 2.1. Then, in Sec. 2.2 we introduce our parametric scattering transform and describe how to differentiating through this parametrized scattering transform in order to learn its parameters with gradient descent approaches. Finally, Sec. 2.3 discussed scattering parameter initialization.

2.1. Scattering Networks

For simplicity, we focus here on 2D scattering networks up to their 2nd order. Subsequent orders can be computed by following the same iterative scheme, but have been shown to yield negligible energy [2]. Given a signal $x(u)$, where u is the spatial position index, we compute the scatterings coefficients S^0x, S^1x, S^2x , of order 0, 1 and 2 respectively. For an integer J , corresponding to the spatial scale of the scattering transform, and assuming an $N \times N$ signal input with one channel, the resulting feature maps are of size $\frac{N}{2^J} \times \frac{N}{2^J}$, with channel sizes varying with the scattering coefficients' order.

To calculate 0th-order coefficients, we consider a low pass filter ϕ_J with a spatial window of scale 2^J , such as a Gaussian smoothing function. We then convolve this filter with the signal, and downsample by a factor of 2^J to obtain $S^0x(u) = x * \phi_J(2^Ju)$. Due to the low pass filtering, high frequency information is discarded here and is recovered in higher order coefficients via wavelets introduced as in a filter bank.

Morlet wavelets are a typical example of filters used in conjunction with the scattering transform, and are defined as

$$\psi_{\sigma,\theta,\xi,\gamma}(u) = e^{-\|R_{\theta,\gamma}(u)\|^2/(2\sigma^2)}(e^{i\xi u'} - \beta), \quad (1)$$

where β is a normalization constant to ensure wavelets integrate to 0 over the spatial domain, $u' = u_1 \cos \theta + u_2 \sin \theta$, and $R_{\theta,\gamma}(u) = \begin{pmatrix} \cos(\theta) & \sin(\theta) \\ \gamma \sin(\theta) & -\gamma \cos(\theta) \end{pmatrix} \begin{pmatrix} u_1 \\ u_2 \end{pmatrix}$. The four parameters can be adjusted and are presented in

Table 1. Parameters of Morlet wavelet

Param	Role	Param	Role
σ	Gaussian window scale	θ	Global orientation
ξ	Frequency scale	γ	Slant

Table 1. From one wavelet $\psi_{\sigma',\theta',\xi',\gamma'}(u)$, a tight frame is obtained by dilating it by factors 2^j , $0 \leq j < J$, and rotating by L angles θ equally spaced over the circle, to get $\{2^{-2j}\psi_{\sigma',\theta',\xi',\gamma'}(2^{-j}R_{\theta,1}(u))\}$, which is then completed with the lowpass ϕ_J . This can be written in terms of the parameters in Table 1 as $\psi_{2^j\sigma',\theta'-\theta,2^{-j}\xi',\gamma'}(u) = \psi(2^{-j}R_{\theta,1}u)$. By slight abuse of notations, we use ψ_λ here, $\lambda = (\sigma_j, \theta, \xi_j, \gamma_j)$, to denote such wavelets indexed by θ and j .

First-order scattering coefficients are calculated by first convolving the input signal with one of the generated complex wavelets (i.e., indexed by the parameters in Table 1) and downsampling the resulting filtered signal by the scale factor 2^{j_1} of the wavelet chosen. Then, a pointwise complex modulus is used to add nonlinearity, and the resulting real signal is smoothed via a low pass filter. Finally, another downsampling step is applied, this time by a factor of 2^{J-j_1} , to obtain an optimally compressed output size. Mathematically, we have

$$S^1x(\lambda_1, u) = |x * \psi_{\lambda_1}| * \phi_J(2^Ju).$$

The resulting feature map has $J \cdot L$ channels, based on the number of wavelets in the generated family.

Second order coefficients are generated in a similar way, with the addition of another cascade of wavelet transform and modulus operator before the low pass smoothing, i.e.,

$$S^2x(\lambda_1, \lambda_2, u) = ||x * \psi_{\lambda_1}| * \psi_{\lambda_2}| * \phi_J(2^Ju).$$

Due to the interaction between the bandwidths and frequency supports of first and second order, only coefficients with $j_1 < j_2$ have significant energy. Hence, the second order output yields a feature map with $\frac{1}{2}J(J-1)L^2$ channels.

2.2. The Parametric Scattering Transform

While traditionally the wavelet filters are fixed to approximate a tight frame, we let the network learn the optimal parameters of each filter. In other words, we constrain our filters to always be Morlet wavelets by only optimizing the parameters in Table 1. To provide such data-driven optimization of scattering parameters, we show here that it is possible to back-propagate through this construction. Namely, we verify the differentiability of this construction by explicitly computing the partial derivatives with respect to these parameters.

First, the \mathbb{R} -linear derivative of the complex modulus $f(z) = |z|$ is $f'(z) = \frac{z}{|z|}$. Next, we show the differentiation of convolution with wavelets with respect to their parameters. For simplicity, we focus here on differentiation of the Gabor portion² of the filter construction from Eq. 1, written as:

$$\begin{aligned} \varphi(u) = & \exp\left(-\frac{1}{2\sigma^2}(u_1^2(\cos^2(\theta) + \sin^2(\theta)\gamma^2) + u_2^2(\cos^2(\theta)\gamma^2 \right. \\ & \left. + \sin^2(\theta)) + 2\cos(\theta)\sin(\theta)u_1u_2(1 - \gamma^2)) \right. \\ & \left. + i\xi(\cos(\theta)u_1 + \sin(\theta)u_2)\right). \end{aligned}$$

Its derivatives with respect to the parameters are

$$\begin{aligned} \frac{\partial \varphi}{\partial \theta}(u) &= \frac{1}{\sigma^2}(u_2 \cos \theta - u_1 \sin \theta)(i\xi\sigma^2 + u_1(\gamma^2 - 1) \cos \theta \\ &\quad + u_2(\gamma^2 - 1) \sin \theta)\varphi(u); \\ \frac{\partial \varphi}{\partial \sigma}(u) &= \frac{1}{\sigma^3}(u_1^2(\cos^2 \theta + \gamma^2 \sin^2 \theta) + u_2^2(\gamma^2 \cos^2 \theta \\ &\quad + \sin^2 \theta) + 2u_1u_2 \cos \theta \sin \theta(1 - \gamma^2))\varphi(u); \\ \frac{\partial \varphi}{\partial \xi}(u) &= i(u_1 \cos \theta + u_2 \sin \theta)\varphi(u); \text{ and} \\ \frac{\partial \varphi}{\partial \gamma}(u) &= -\frac{1}{\sigma^2}(u_1^2\gamma \sin^2 \theta + u_2^2\gamma \cos^2 \theta \\ &\quad - 2u_1u_2\gamma \cos \theta \sin \theta)\varphi(u). \end{aligned}$$

Finally, the derivative of the convolution with such filters is given by $\frac{\partial}{\partial \zeta}(f * \varphi)(t) = \int f(t-u) \frac{\partial \varphi}{\partial \zeta}(u) du$ where ζ is any of the filter parameter from Table 1. It is easy to verify that these derivations can be chained together to propagate through the scattering cascades defined in Sec. 2.1. We can now learn these jointly with other parameters in an end-to-end differentiable architecture.

2.3. Initialization

To evaluate the ability of data-driven learning to tune the scattering parameters, we consider two initializations and study their impact on resulting performance in both learned and nonlearned settings. First, a tight frame initialization follows common implementations of the scattering transform by setting $\sigma_{j,\ell} = 0.8 * 2^j$, $\xi_{j,\ell} = \frac{3\pi}{4}2^{-j}$, and $\gamma_{j,\ell} = \frac{4}{L}$

for $j = 1, \dots, J$, $\ell = 1, \dots, L$, while for each j , we set $\theta_{j,\ell}$ to be equally spaced on $[0, 2\pi)$. Second, as an alternative, we consider a random initialization where these parameters are sampled as $\sigma_{j,\ell} \sim \log(U[e, e^5])$, $\xi_{j,\ell} \sim U[0.5, 1]$, $\gamma_{j,\ell} \sim U[0.5, 1.5]$, and $\theta_{j,\ell} \sim U[0, 2\pi]$. That is, orientations are selected uniformly at random on the circle, the filter width σ is selected using an exponential distribution across available scales and the spatial frequency ξ is chosen to be in the interval $[0.5, 1]$, which lies in the center of the feasible range between aliasing ($> \pi$) and the fundamental frequency of the signal size ($2\pi/N$ where N is the number of pixels). Finally, we select the *slant* variable governing the aspect ratio to vary around the spherical setting of 1.0, with a bias towards stronger orientation selectivity (0.5) compared to lesser orientation selectivity (1.5).

3. EXPERIMENTAL SETUP

To evaluate our approach, we consider an architecture inspired by [9], where scattering is combined with a Wide Residual Network [11] of depth 16 and width 8, henceforth denoted WRN; and a simpler one, denoted LL, where scattering is followed by a linear model – a commonly used evaluation for learned and designed representations [12, 9]. In both cases, we compare learned parametric scattering networks (LS) to fixed ones (S), yielding four combinations: LS + WRN, S + WRN, LS + LL, and S + LL. The WRN configurations provide a setting comparable to previous work on hybrid scattering (i.e., the S + WRN setting is equivalent to [9]), and give an estimate of the peak performance of parametric scattering networks. The LL configurations are used to evaluate the linear separability of the obtained scattering representations and have the added benefit of providing a more interpretable model.

When using learned and fixed scattering, we consider both random and tight frame (TF) initializations, as discussed in Sec. 2.3. The fixed scattering models determined by the TF construction are equivalent to traditional scattering transforms. Together with the four aforementioned architectures, this yields eight scattering configurations. Finally, we also compare our approach to a fully learned WRN (with no scattering priors) applied directly to input data, thus giving a total of nine reported models in Tables 2-4.

In all configurations, a batch normalization layer with learnable affine parameters is added after all scattering layers. The classification is done via a softmax layer yielding the final output. All models are trained using cross-entropy loss, minimized by stochastic gradient descent with momentum of 0.9. Weight decay is applied to the linear model and to the WRN. The learning rate is scheduled according to one cycle policy [13], which improves convergence during optimization, especially in the small data regime, due to its so-called super convergence (see [13] for further details).³

²It is not difficult to extend this derivation to Morlet wavelets, but the resulting expressions are rather cumbersome and left out for brevity.

³The scheduler div factor is always set to 25, while learning rate is tuned.

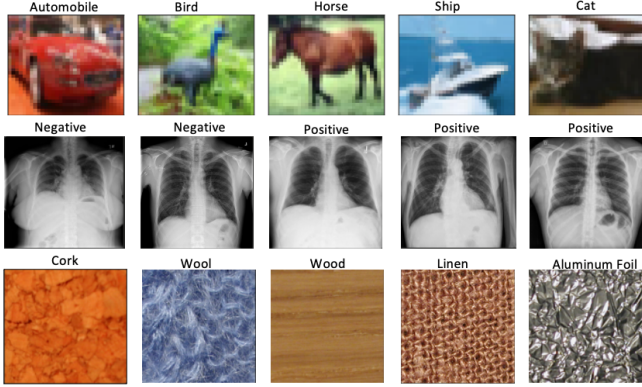


Fig. 2. Samples from the three datasets: CIFAR-10 (top), COVIDx CRX-2 (middle), and KTH-TIPS2 (bottom).

4. RESULTS

Our empirical evaluations are based on three image datasets, illustrated in Fig. 2. Following the evaluation protocol from [9] we subsample each dataset at various sample sizes in order to showcase the performance of scattering-based architectures in the small data regime. CIFAR-10 and KTH-TIPS2 are natural image and texture recognition datasets (correspondingly). They are often used as general-purpose benchmarks in similar image analysis settings [14, 8]. COVIDx CRX-2 is a dataset of X-ray scans for COVID-19 diagnosis; its use here demonstrates the viability of our parametric scattering approach in practice, e.g., in medical imaging applications.

To obtain comparable and reproducible results, we control for deterministic GPU behaviour and assure that each model is initialized the same way for the same seed. Furthermore, we use the same set of seeds for models evaluated on the same number of samples. For instance, the TF learnable hybrid with linear model would be evaluated on the same ten seeds as the fixed tight frame hybrid with linear model when trained on 100 samples of CIFAR-10. Some error is inevitable when subsampling datasets, hence all our figures include averages and standard error calculated over the different seeds.

4.1. CIFAR-10

CIFAR-10 is a popular benchmark in computer vision, consisting of 60,000 images of size $32 \times 32 \times 3$ from ten classes. The train set contains 50,000 class-balanced samples, while the test set contains the remaining images. In our experiments, we train on a small random subset of the training data, but always test on the entire test set as per [9]. The training set is augmented with horizontal flipping, random cropping, and pre-specified autoaugment [15] for CIFAR-10. We used [15] to showcase the best possible small sample results.

Table 2 reports the evaluation of our learnable scattering approach on CIFAR-10 with training sample sizes of 100, 500, 1K, and 50K. The hybrid linear models were trained using a max learning rate of 0.06 and a div factor of 25 for

Table 2. CIFAR-10 mean accuracy and std. error over 10 seeds, with $J = 2$ and multiple training sample sizes. Learnable scattering with TF initialization improves performance for all architectures, showing benefits even for small sample sizes, while randomly-initialized scattering requires more training data to reach similar improvements. We note that the number of parameters differs between architectures.

Init.	Arch.	100 samples	500 samples	1000 samples	All
TF	LS+LL†	37.84 \pm 0.57	52.68 \pm 0.31	57.43 \pm 0.17	69.57 \pm 0.1
TF	S+LL	36.01 \pm 0.55	48.12 \pm 0.25	53.25 \pm 0.24	65.58 \pm 0.04
Rand	LS+LL†	34.81 \pm 0.6	49.6 \pm 0.39	55.72 \pm 0.39	69.39 \pm 0.41
Rand	S+LL	29.77 \pm 0.47	41.85 \pm 0.41	46.3 \pm 0.37	57.72 \pm 0.1
TF	LS+WRN†	43.6 \pm 0.87	63.13 \pm 0.29	70.14 \pm 0.26	93.61 \pm 0.12
TF	S+WRN	43.16 \pm 0.78	61.66 \pm 0.32	68.16 \pm 0.27	92.27 \pm 0.05
Rand	LS+WRN†	41.42 \pm 0.65	59.84 \pm 0.40	67.4 \pm 0.28	93.36 \pm 0.19
Rand	S+WRN	32.08 \pm 0.46	46.84 \pm 0.21	52.76 \pm 0.33	85.35 \pm 1.06
	WRN	38.78 \pm 0.72	62.97 \pm 0.41	71.37 \pm 0.31	95.7 [9]

†: ours TF: Tight Frame LS: Learnable Scattering S: Scattering

params : 156k for S+LL; 155k for LS+LL; 22.6M for S+WRN; 22.6M LS+WRN; and 22.3M for just WRN

all parameters on 5K, 1K, 500, and 500 epochs for 100, 500, 1K, 50K samples respectively. The hybrid WRN models were trained using a max learning rate of 0.1 and a div factor of 25 on 3K, 2K, 1K, and 200 epochs for 100, 500, 1K, and 50K samples respectively. As shown in Table 2, TF-initialized models outperform others in limited sample settings. Moreover, randomly-initialized fixed scattering perform the worst, while randomly-initialized learned models yield performance gains relative to TF ones as the sample size increases.

Among the linear models, our TF-initialized learnable scattering one significantly outperforms all others in few sample settings. This demonstrates that learnable scattering networks obtain a more linearly separable representation than their fixed counterparts, perhaps by building greater dataset-specific intra-class invariance. Moreover, in the very small sample regime of 100 training samples performance of the linear model on learned scattering rivals that of a highly non-linear learned CNN. Interestingly, when comparing TF learnable to fixed, we observe that the relative performance gain of learning increases from 100 samples (1.83) to 500 samples (4.56), yet it remains relatively constant for 500, 1K, and 50K sample settings, indicating that perhaps 500 samples are sufficient to tune a scattering representation when starting from TF initialization. In contrast, randomly-initialized learnable scattering only improves beyond the fixed tight frame after 500 samples, and only achieves similar performance to TF learnable when trained on the whole dataset. These results suggested the TF initialization, derived from rigorous signal processing principles, is empirically beneficial as a starting point in the very few sample regime, but can be improved upon by learning. Figure 1 shows the real part of the wavelet filters before and after optimization on the entire training set. Scales and slants of TF-initialized filters change substantially but their orientations remain approximately the same. For random initialization, all filters undergo major transformations in orientation, scale, and slant.

Table 3. COVIDx CRX-2 mean accuracy & std. error over 10 seeds, with $J = 3$ and multiple training sample sizes. Highest mean acc. is obtained with learnable scattering followed by WRN, trained on 1000 images. We note that the numbers of parameters differs between architectures.

Init.	Arch.	100 samples	500 samples	1000 samples
TF	LS+LL†	74.8 ± 1.65	83.1 ± 0.84	84.58 ± 0.79
TF	S +LL	75.48 ± 1.77	83.58 ± 0.91	86.18 ± 0.49
Rand	LS+LL†	73.15 ± 1.35	82.33 ± 1.1	84.73 ± 0.59
Rand	S +LL	74.25 ± 0.86	82.53 ± 0.76	85.43 ± 0.51
TF	LS+WRN†	78.1 ± 1.62	86.15 ± 0.63	89.65 ± 0.42
TF	S +WRN	76.23 ± 2	86.5 ± 0.66	89.13 ± 0.36
Rand	LS+WRN†	74.86 ± 1.22	84.15 ± 0.79	87.63 ± 0.55
Rand	S +WRN	75.4 ± 1.03	83.75 ± 0.58	87.48 ± 0.61
	WRN	69.15 ± 1.13	80.04 ± 2.41	87.81 ± 1.37

†: ours; TF: Tight Frame LS: Learnable Scattering S: Scattering
params : 189K for LS/S+LL; 23.05M for LS/S+WRN; 22.3M for WRN

Among the WRN hybrid models, the TF-initialized learnable scattering network performs best. However, the lone WRN outperforms our model in 1,000 sample and 50,000 sample settings. The relative performance gains of TF learnable over TF fixed are much smaller here when compared to the linear hybrid model. We interpret this as an indication that some performance was gained due to the ability of learnable scattering to linearly separate data when no other source of nonlinear processing is present in the model. However, TF learnable still improves over TF fixed when paired with a WRN, indicating some loss of information in the fixed scattering representation is mitigated by data-driven tuning or optimization. Note that S+WRN corresponds to the setting of [9], with our higher results in this setting due to use of more data augmentation. We confirmed when using the latter’s data augmentation performance gains for LS+WRN are similar. For example in the 1000 sample case when using the augmentation of [9] learnable scattering obtains 61.8% accuracy vs 60.3% averaged over 8 runs.

4.2. COVIDx CRX-2

COVIDx CRX-2 is a two class (positive and negative) dataset of $1024 \times 1024 \times 1$ chest X-Ray images of COVID-19 patients [16]. The train set contains 15,951 unbalanced images, while the test set contains 200 positive and 200 negative. In our experiments, we always train on a class-balanced subset of the training set. We resize the images to 128×128 and train our network with random crops of 96×96 pixels. The only data augmentation we use is random horizontal flipping. All scattering networks use a spatial scale $J=3$.

Table 3 reports our evaluation on COVIDx CRX-2, with training on sample sizes of 100, 500, and 1K images using the same protocol as CIFAR-10. All linear models were trained on 400 epochs using a max learning rate of 0.06 linear layer parameters and 0.1 for scattering parameters. The hybrid WRN models were trained on 200 epochs using a max learning rate of 0.1. For the linear model we observe that

Table 4. KTH-TIPS2 mean accuracy and std. error over 16 runs with $J = 3$. Learning the parameters brings significant improvement in both LL or WRN configurations. Even with random initialization, trainable scattering yields better performance than nonlearnable tight-frame scattering.

Initialization	Architecture	Accuracy	Num Params
TF	LS+LL†	66.83 ± 0.94	1.8M
TF	S +LL	63.91 ± 0.57	1.8M
Random	LS+LL†	65.98 ± 0.73	1.8M
Random	S +LL	60.42 ± 0.34	1.8M
TF	LS+WRN†	66.46 ± 1.09	23.1M
TF	S +WRN	63.77 ± 0.59	23.1M
Random	LS+WRN†	67.35 ± 0.51	23.1M
Random	S +WRN	65.05 ± 0.38	23.1M
	WRN	51.24 ± 1.37	22.3M

†: ours; TF: Tight Frame LS: Learnable Scattering S: Scattering

the tight frame initialization performs slightly better than the learned evaluation, although we note that the error bars overlap in most of the settings. This suggests that the tight frame is already near optimal for this data. We also observe that even random initialization can give reasonable results, exceeding the performance of CNNs on this data in the small sample regime. When combined with a CNN, the scattering yields the best performance for 100 and 1000 samples. Similar to CIFAR-10, this benchmark exhibits the advantages of using the TF initialization. Indeed, as a whole, TF configurations exhibit higher accuracy than randomly-initialized ones, while also showing that it can be improved upon by learning in many cases. Finally, we observe that the WRN alone performs worse than the other architectures, demonstrating the effectiveness of the scattering prior (i.e., using learnable or nonlearnable parameters) in the small data regime.

4.3. KTH-TIPS2

KTH-TIPS2 is a texture dataset containing 4,752 images from 11 material classes. Each class is divided into four *samples* (108 images each) of different scales. Using the standard protocol, we train the model on one *sample* (11×108 images), while the rest are used for testing [17]. In total, each training set contains 1,188 images. We resize these images to 200×200 and train our network with random crops of 128×128 pixels. The training data is augmented with random horizontal flips and random rotations. All scattering networks use a spatial scale of 3. We set the maximum learning rate of the scattering parameters to 0.1 while it is set to 0.001 for all other parameters. All hybrid models are trained with a mini-batch size of 128. However, the hybrid linear models are trained for 250 epochs, while the hybrid WRN models are trained for 150 epochs. We evaluate each model, training it with 4 different seeds on each *sample*, amounting to 16 total runs for each of the 9 models we evaluate.

Table 4 reports classification accuracies for KTH-TIPS2. Among the linear hybrid models, we observe that optimiz-

ing the scattering parameters improves performance. Indeed, the TF learnable model achieves the highest accuracy, while the random learnable model is a close second. We observe that learning the filters' parameters brings a significant improvement over fixing them: 2.92% and 3.71% for TF and random respectively. We also see that the fixed and randomly-initialized models perform the worst, showing that even poorly initialized filters can effectively be optimized. Altogether, these results further corroborate our previous findings, notably that all filters can effectively be optimized, but that beyond being valuable for fixed scattering networks, the tight frame initialization also helps the learning process.

Out of all the WRN hybrid models, the random learnable model achieves the highest accuracy and is the only one to improve over its linear counterpart. This is contrary to our findings for CIFAR-10 and COVIDx CRX-2, namely that tight frame is best and the WRN always improves over the linear layer. We hypothesize that this is due to a couple of factors: residual networks perform poorly at texture discrimination and it may be difficult to escape the TF local minimum. While its relative performance in 1000 sample CIFAR-10 and xray settings (similar to the 1,188 samples used here) is very competitive, the lone WRN (i.e., without parametric scattering priors) performs extremely poorly relative to hybrid models on KTH-TIPS2, supporting our hypothesis. Furthermore, TF aids optimization throughout, yet fails to do the same for textures. This may be due to texture discrimination requiring different invariance properties [2] than the other datasets, leading the TF-initialized networks to remain stuck at local minima, while the random learnable models are freer to roam the optimization space. As a final remark, we note that while WRN increases the performance in some cases, it also significantly increases the total number of parameters, therefore exhibiting a tradeoff between performance and model complexity.

5. CONCLUSION

This work demonstrates the competitive results of learning Morlet wavelet filter parameters by differentiating through scattering networks. When trained on subsamples of CIFAR-10, learnable scattering with TF initialization improves performance for all architectures. On X-ray scans, improvements are less significant, though our method is still the most accurate with the LS+WRN configuration and TF initialization, demonstrating the real-world viability of our approach. On texture data, learning the parameters yields significant improvement with both linear and WRN downstream layers. Overall, we show that, in small sample settings, learned versions of the scattering transform yield significant performance gains over the nonlearned ones. Moreover, the standard tight frames are not always necessary to extract effective representations, as even with randomly-initialized filters, our approach yields comparable or better results.

References

- [1] S. Mallat, "Group invariant scattering," *Commun. Pure Appl. Math.*, vol. 65, no. 10, pp. 1331–1398, 2012.
- [2] J. Bruna and S. Mallat, "Invariant scattering convolution networks," *IEEE Trans. Pattern Anal. Mach. Intell.*, vol. 35, no. 8, pp. 1872–1886, 2013.
- [3] S. Mallat, "Understanding deep convolutional networks," *Phil. Trans. of the Royal Society A*, vol. 374, no. 2065, pp. 20150203, 2016.
- [4] D.G. Lowe, "Distinctive image features from scale-invariant keypoints," *Int. J. Comput. Vis.*, vol. 60, no. 2, pp. 91–110, 2004.
- [5] E. Oyallon, E. Belilovsky, and S. Zagoruyko, "Scaling the scattering transform: Deep hybrid networks," in *Proc. of ICCV*, 2017, pp. 5618–5627.
- [6] J. Andén, V. Lostanlen, and S. Mallat, "Joint time-frequency scattering for audio classification," in *Proc. of MLSP*, 2015, pp. 1–6.
- [7] M. Eickenberg, G. Exarchakis, M. Hirn, S. Mallat, and L. Thiry, "Solid harmonic wavelet scattering for predictions of molecule properties," *J. Chem. Phys.*, vol. 148, no. 24, pp. 241732, 2018.
- [8] L. Sifre and S. Mallat, "Rotation, scaling and deformation invariant scattering for texture discrimination," in *Proc. of CVPR*, 2013, pp. 1233–1240.
- [9] E. Oyallon, S. Zagoruyko, G. Huang, N. Komodakis, S. Lacoste-Julien, M.B. Blaschko, and E. Belilovsky, "Scattering networks for hybrid representation learning," *IEEE Trans. Pattern Anal. Mach. Intell.*, vol. 41, no. 9, pp. 2208–2221, 2018.
- [10] N. Bendre, H. Terashima-Marín, and P. Najafirad, "Learning from few samples: A survey," arXiv:2007.15484, 2020.
- [11] S. Zagoruyko and N. Komodakis, "Wide residual networks," in *Proc. of BMVC*, 2016, pp. 87.1–87.12.
- [12] E. Oyallon and S. Mallat, "Deep roto-translation scattering for object classification," in *Proc. of CVPR*, 2015, pp. 2865–2873.
- [13] L. Smith and N. Topin, "Super-convergence: Very fast training of neural networks using large learning rates," in *AI & ML for Multi-Domain Oper. App.*, 2019.
- [14] I. Azuri and D. Weinshall, "Generative latent implicit conditional optimization when learning from small sample," in *Proc. of ICPR*, 2021, pp. 8584–8591.
- [15] E.D. Cubuk, B. Zoph, D. Mané, V. Vasudevan, and Q.V. Le, "Autoaugment: Learning augmentation policies from data," in *Proc. of CVPR*, 2019, pp. 113–123.
- [16] L. Wang, Z.Q. Lin, and A. Wong, "COVID-Net: a tailored deep convolutional neural network design for detection of COVID-19 cases from chest X-ray images," *Scientific Reports*, vol. 10, pp. 19549, 2020.
- [17] Y. Song, F. Zhang, Q. Li, H. Huang, L.J. O'Donnell, and W. Cai, "Locally-transferred fisher vectors for texture classification," in *Proc. of ICCV*, 2017, pp. 4912–4920.